








# Ultraviolet photodetectors and readout based on a-IGZO semiconductor technology

Yannick Schellander, SID Student Member<sup>1,2</sup>  | Marius Winter<sup>1</sup>  |  
 Maurice Schamber<sup>3</sup>  | Fabian Munkes<sup>3</sup>  |  
 Patrick Schalberger, SID Member<sup>1,2</sup>  | Harald Kuebler<sup>2,3</sup>  | Tilman Pfau<sup>2,3</sup>  |  
 Norbert Fruehauf, SID Member<sup>1,2</sup>

<sup>1</sup>Institute for Large Area Microelectronics, University of Stuttgart, Stuttgart, Germany

<sup>2</sup>Research Center SCoPE, University of Stuttgart, Stuttgart, Germany

<sup>3</sup>5th Institute of Physics, University of Stuttgart, Stuttgart, Germany

## Correspondence

Yannick Schellander, Institute for Large Area Microelectronics, University of Stuttgart, Stuttgart, Germany.  
 Email: [yschellander@igm.uni-stuttgart.de](mailto:yschellander@igm.uni-stuttgart.de)

## Funding information

Deutsche Forschungsgemeinschaft, Grant/Award Number: 431314977/GRK2642

## Abstract

In this work, real-time ultraviolet photodetectors are realized through metal–semiconductor–metal (MSM) structures. Amorphous indium gallium zinc oxide (a-IGZO) is used as semiconductor material and gold as metal electrodes. The readout of an individual sensor is implemented by a transimpedance amplifier (TIA) consisting of an all-enhancement a-IGZO thin-film transistor (TFT) operational amplifier and a switched capacitor (SC) as feedback resistance. The photosensor and the transimpedance amplifier are both manufactured on glass substrates. The measured photosensor possesses a high responsivity  $R$ , a low response time  $t_{\text{RES}}$ , and a good noise equivalent power value  $NEP$ .

## KEYWORDS

detection of ambient light, dual gate a-IGZO thin-film transistors, non-visible spectrum optical sensing, operational amplifier, sensor integration, sensors under displays, switched capacitor, transimpedance amplifier, UV photosensors

## 1 | INTRODUCTION

Ultraviolet photodetectors attracted attention because of their wide range of applications in fire monitoring, space communication or biomedicine.<sup>1,2</sup> Standard silicon-based photodiodes have low responsivities in the ultraviolet wavelength region. The reason for this is the relatively low bandgap of 1.12 eV.<sup>3</sup> One way to achieve highly responsive sensors for ultraviolet wavelengths is to use semiconductor materials with much higher bandgaps. Amorphous indium gallium zinc oxide (a-IGZO) is a suitable candidate because of its bandgap of 3.05 eV. This

should allow the detection of light with wavelengths lower than 400 nm.<sup>4,5</sup> It also follows from this that the sensors are not affected by visible light. Therefore, possible disturbing background light does not have to be filtered out. In this work, a photoresistor in a metal–semiconductor–metal design is presented as photodetector structure. The fabricated photosensors show responsivity values up to 120 A/W and response times in the millisecond range. The generated current by an individual sensor is measured by a transimpedance amplifier realized through an operational amplifier consisting of all-enhancement a-IGZO TFTs and a switched capacitor.

This is an open access article under the terms of the [Creative Commons Attribution-NonCommercial-NoDerivs](https://creativecommons.org/licenses/by-nc-nd/4.0/) License, which permits use and distribution in any medium, provided the original work is properly cited, the use is non-commercial and no modifications or adaptations are made.

© 2023 The Authors. *Journal of the Society for Information Display* published by Wiley Periodicals LLC on behalf of Society for Information Display.

Hence, both the sensor and the readout are fabricated on glass substrates. In the near future both should be fabricated on the same substrate. The advantage of this is that the readout is located extremely close to the photosensor, which leads to a reduction of the collected noise, resulting in an improvement of the signal-to-noise ratio. The combination of sensor and readout on the same substrate is suitable for applications like sensors integrated into displays or detection of ambient light. Moreover, fabricating detectors using thin-film technology on glass is a good choice for array applications because of the easy scalability. At first the layer structure and the fabrication process of the needed TFTs for the readout is discussed. Afterwards, the electrical properties like input and output characteristics of the created TFTs are analyzed. Next the manufacturing of the photosensors is described. Then the fabricated photosensors are characterized. Subsequently, the single elements (switched capacitor and operational amplifier) of the transimpedance amplifier are treated. The properties of the presented TIA are also investigated. The main part of this paper is dealing with the performance analysis of the presented photosensor-transimpedance amplifier combination.

## 2 | THIN-FILM TRANSISTOR LAYER STRUCTURE

The layer structure (cross-section view) of the enhancement mode TFTs investigated in this work is shown in Figure 1. At first a 70 nm, MoTa layer is deposited using DC magnetron sputtering. Afterwards, the layer is structured to form the bottom gate. Next a double layer consisting of 175 nm SiN and 50 nm SiO<sub>x</sub> is placed as bottom dielectric. This layer is created by plasma enhanced chemical vapor deposition (PECVD) at 280°C. The structuring of this layer is done by reactive-ion etching (RIE). Then the drain and source are manufactured as a double layer of 70 nm MoTa and 50 nm ITO. The

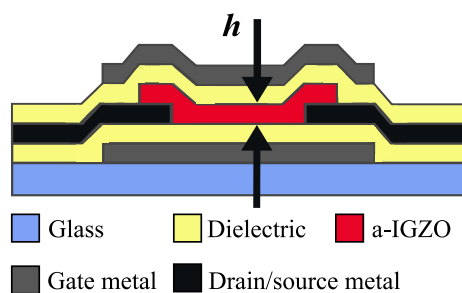


**FIGURE 1** Cross-section view: Enhancement mode dual gate amorphous indium gallium zinc oxide thin-film transistor (a-IGZO TFT) with a channel thickness  $h$  of 40 nm.

fabrication process is adjusted in such a way that only ITO is in direct contact with the later deposited a-IGZO channel. Before the IGZO layer is added to the layer stack, the substrates are tempered for 1 h at 250°C. This tempering step has the purpose to increase the conductivity of the ITO layer. An ohmic contact to the semiconductor should be created. a-IGZO is deposited using RF magnetron sputtering from a solid state (1:1:1 mol %)-IGZO target. A layer thickness of 40 nm is chosen. After the creation of the semiconductor channel, the substrates are annealed for 2 h at 300°C. To isolate the top gate, a layer of 130 nm SiO<sub>x</sub> is used. This layer is placed via PECVD at 250°C. The temperature is decreased in comparison with the deposition of the bottom dielectric to minimize negative influences on the semiconductor. As top gate a double layer of 70 nm MoTa and 50 nm ITO is used. As the last step of the manufacturing the transistors are tempered overnight (around 16 h to 18 h) at 250°C. During the tempering, electrons are bound and the conductivity is decreased. This yields a slightly positive threshold voltage of the produced dual gate a-IGZO transistors.

## 3 | THIN-FILM TRANSISTOR CHARACTERISTICS

In Figure 2, the input and output characteristics of four identically constructed transistors are shown. In the cut-off region, currents lower than 70 pA are detected. The cut-off currents are slightly increased to common known a-IGZO TFTs. This has no negative influence on the created transimpedance amplifier. The transistors have threshold voltages  $V_{TH}$  in the range from 2.53 V to 2.77 V. Thus, enhancement mode TFTs are created by the presented process. The measured effective field-effect mobilities  $\mu$  are ranging from 8.93 cm<sup>2</sup>/(Vs) to 10.05 cm<sup>2</sup>/(Vs). The output curves  $I_D(V_{DS})$  show that for  $V_{DS}$  greater than or equal to  $V_{GS}$  the drain current  $I_D$  saturates. Under this condition the TFTs can act as diode loads.

## 4 | PHOTODIODE LAYER STRUCTURE

In Figure 3, the cross-section view of the layer structure of the photosensor is shown. First, a dielectric layer (150 nm SiO<sub>x</sub>) is deposited on the glass substrate to create a buffer layer. In the future when the sensor and the readout are manufactured on the same substrate, this layer should separate the gold electrodes from the top gate of the TFTs. Of course, a VIA at the right position is

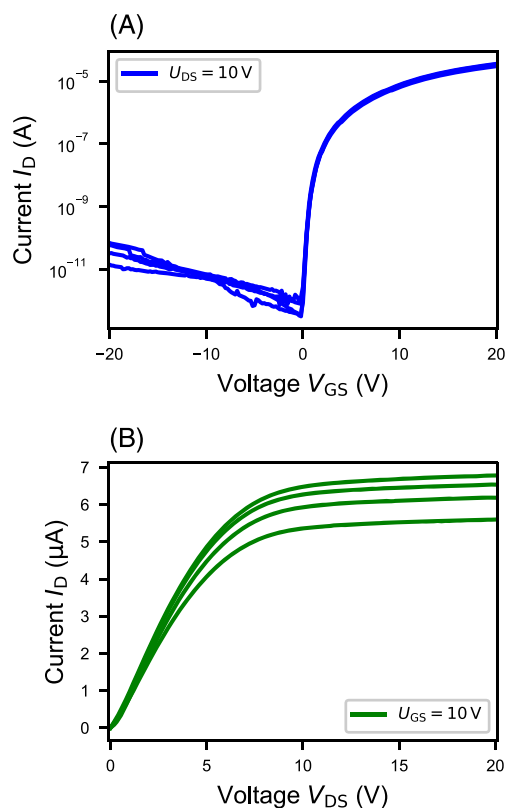


**FIGURE 2** (A) Input characteristics  $I_D(V_{GS})$  of dual gate amorphous indium gallium zinc oxide thin-film transistors (a-IGZO TFTs) with a channel width  $w = 10 \mu\text{m}$ , a channel length  $l = 10 \mu\text{m}$ , and a channel thickness  $h = 40 \text{ nm}$ . (B) Output characteristics  $I_D(V_{DS})$  for a gate-source voltage  $V_{GS} = 10 \text{ V}$ .

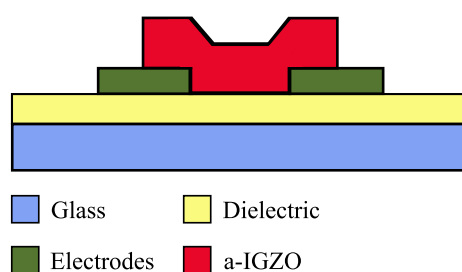


**FIGURE 3** Cross-section view: photodetector (metal–semiconductor–metal [MSM]–structure) with an active semiconductor geometry of  $w = 100 \mu\text{m}$ ,  $l = 10 \mu\text{m}$  and thickness  $h = 140 \text{ nm}$ . The electrodes are realized by a chromium–gold double layer.

needed to connect the sensor and the readout. Next a double layer consisting of 20 nm chromium and 75 nm gold is used as metal electrodes. The chromium acts as adhesive layer. Because of the working function of gold, Schottky barriers are forming between the gold electrodes and the semiconductor. As photosensitive material a-IGZO with a layer thickness of 140 nm is used.

Measurements with different thicknesses (Figure 4) illustrate that with increasing thickness  $h$ , the response time  $t_{\text{RES}}(\text{down})$  of the photodetectors decrease. For thicknesses  $h$  larger than 100 nm the response time  $t_{\text{RES}}(\text{down})$  is in the millisecond region. The lowest measured value is 11.4 ms.

## 5 | PHOTODIODE CHARACTERIZATION

The influence of UV light on the conductivity of a-IGZO can be used to detect wavelengths lower than the semiconductor's bandgap. Metal–semiconductor–metal structures are one possibility to realize photodetector devices. An MSM diode includes two Schottky junctions that are connected back-to-back in series.<sup>6</sup> Gold electrodes are connected through a semiconductor channel with 100  $\mu\text{m}$  width, 10  $\mu\text{m}$  length, and 140 nm thickness. The channel geometry has an influence on the dark current and on the current under light exposure. Larger active sensor areas lead to higher currents which can be detected more easily. But with increasing size, the resolution of a possible sensor array is decreased. In Figure 5, the  $I$ - $V$  curves of four identical MSM-structures with and without UV light exposure (385 nm) are illustrated. Without light exposure, the measured currents are below 0.27 nA. For every detector, the lowest current is measured for a voltage  $V$  of 0 V. The light exposure leads to a current increase of 0.52  $\mu\text{A}$ . The highest current  $I$  is measured at the voltage  $V = 20 \text{ V}$ . In general, it can be seen that with and without light exposure the current  $I$  increases with rising voltage  $V$ . Theoretically, the detectors are designed symmetrically, which should lead to symmetrical  $I$ - $V$  curves. Slightly deviations may be caused by manufacturing imperfections, which lead to different Schottky barrier strengths at the two electrode

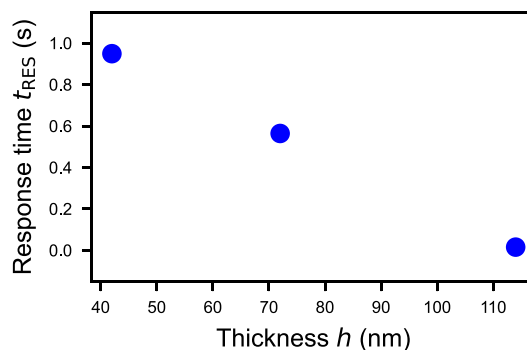


**FIGURE 4** Response time  $t_{\text{RES}}(\text{down})$  of metal–semiconductor–metal (MSM)–structure photodetectors depending on the semiconductor thickness  $h$ .

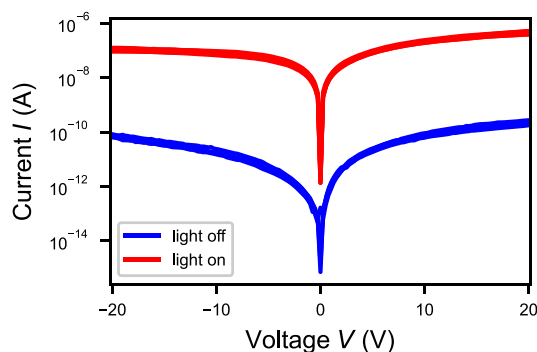


FIGURE 5  $I$ - $V$  curves of the amorphous indium gallium zinc oxide (a-IGZO) photodetectors with and without UV light exposure (385 nm).

semiconductor interfaces. The responsivity  $R = (I_{\text{LIGHT}} - I_{\text{DARK}})/P$  describes how strong the increase in the current ( $I_{\text{LIGHT}}$ : current under light exposure and  $I_{\text{DARK}}$ : dark current) is depending on the light power  $P$  on the sensor.<sup>7</sup> It is the conversion efficiency from optical input into electrical output. The responsivity  $R$  depends on the wavelength  $\lambda$ , light power  $P$ , voltage between the electrodes  $V$ , and temperature  $T$ . In Figure 6 the dependency on voltage  $V$  and light power  $P$  are shown. With increasing voltage  $V$ , the responsivity  $R$  increases. It is expected that at a critical voltage the semiconductor will be damaged due to heating caused by the high current flow. In contrast the responsivity  $R$  decreases for increasing light power  $P$ . Furthermore, the created sensors have a detection limit, which represents the lowest light power that can be detected. The highest measured responsivity  $R = 120$  A/W was taken at room temperature for a voltage of  $V = 30$  V and a light power of  $P = 3.5$  nW reaching the sensor. In comparison with standard silicon-based photodiodes the sensors, show improved responsivity.<sup>8</sup> The noise equivalent power  $NEP$  is a common metric that quantifies a photodetector's sensitivity.<sup>9</sup> It is defined as the input signal power that results in a signal-to-noise ratio  $SNR$  of one per 1 Hz output bandwidth. In Figure 7, the signal-to-noise ratio  $SNR$  depending on the light power  $P$  at an output bandwidth of 1 Hz is shown. As expected, the  $SNR$  increases for increasing light power  $P$ . Because of the chosen bandwidth of 1 Hz the  $NEP$  value is equal to the light power  $P$  resulting in an  $SNR$  of one. For the presented sensor, the extracted  $NEP$  is roughly  $0.2$  nW/ $\sqrt{\text{Hz}}$ .

## 6 | SWITCHED CAPACITOR

In the temporal average a periodically switched capacitor (SC) behaves like an ohmic resistance. One capacitor  $C$

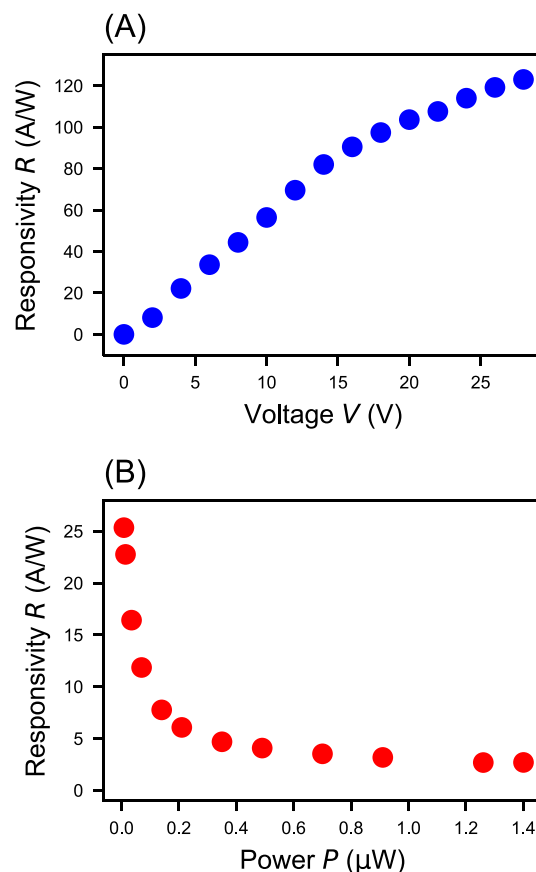


FIGURE 6 (A) Responsivity  $R$  depending on the voltage between the electrodes  $V$ . A light power  $P = 3.5$  nW is illuminating the sensor. (B) Responsivity  $R$  depending on the light power on the sensor  $P$ . The voltage  $V$  between the electrodes is set to 5 V.

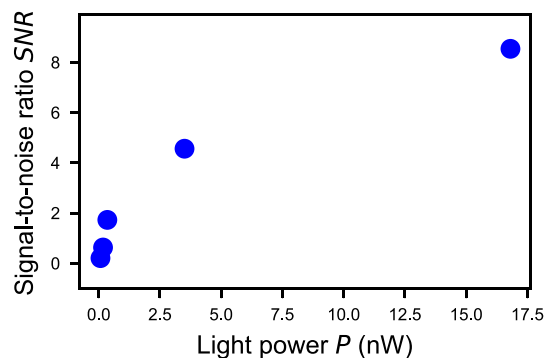


FIGURE 7 Signal-to-noise ratio  $SNR$  depending on the light power  $P$  at an output bandwidth of 1 Hz.

which is switched by four TFTs is shown in Figure 8. In the presented manufacturing process, the needed capacitors are realized by overlapping areas of the drain/source layer with the top gate layer. The top dielectric (130 nm SiOx) separates the metal electrodes of the capacitors. The capacitor value can be calculated as  $C = \epsilon_0 \cdot \epsilon_r \cdot A/$

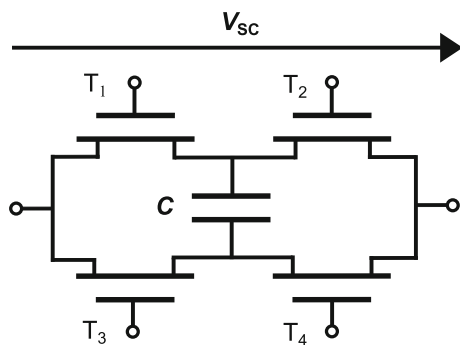


FIGURE 8 Switched capacitor (SC) consisting of four dual gate thin-film transistors (TFTs) with a channel width  $w = 10 \mu\text{m}$  and channel length  $l = 10 \mu\text{m}$  and a single capacitor  $C = 1.4 \text{ pF}$ .

$d$ ,<sup>10</sup> where  $A$  is the overlapping area of the metal layers,  $d$  is the thickness, and  $\epsilon_0 \cdot \epsilon_r$  the permittivity of the dielectric. Every cycle, the voltage on the capacitor is switched from  $V_{\text{SC}}$  to  $-V_{\text{SC}}$  and back. Per cycle, a charge  $Q_{\text{SC}} = 4 C \cdot V_{\text{SC}}$  is flowing. In the temporal mean, this leads to a current  $I_{\text{SC}} = 4 C \cdot V_{\text{SC}} \cdot f_{\text{SC}}$ , respectively, a resistance  $R_{\text{SC}} = 1 / (4 \cdot C \cdot f_{\text{SC}})$ .<sup>11</sup> This illustrates that the resistance  $R_{\text{SC}}$  of a switched capacitor can be adjusted by the switching frequency  $f_{\text{SC}}$ . In Figure 9, experimental data are compared with the theoretical curve. A good agreement can be observed. Furthermore, the possibility to create a resistance of up to  $26.58 \text{ M}\Omega$  is proven. To realize even higher resistances, it would be advantageous to use lower capacitor values. The use of a switched capacitor as feedback resistor in a transimpedance amplifier is beneficial because the  $I$ - $V$  conversion gain of the transimpedance amplifier can easily be adapted to the strength of the measuring signal.

## 7 | ALL-ENHANCEMENT TFT OPERATIONAL AMPLIFIER

The discussed operational amplifier design consists of 19 enhancement mode TFTs and one capacitor  $C = 10 \text{ pF}$ .<sup>12–14</sup> In Figure 10, the circuit diagram is presented. The geometries of all transistors are listed in Table 1. Five different geometries are used. The operational amplifier design can be better understood if the different stages and their functions are discussed individually. The input stage is a differential amplifier ( $T_1, T_2, T_3, T_4$ , and  $T_9$ ). The output voltage of the differential amplifier is the amplified potential difference between the two inputs  $V_{\text{in},+}$  and  $V_{\text{in},-}$ . The needed bias voltage to control the current source ( $T_9$ ) of the input stage is created by an nMOS voltage divider ( $T_5$  and  $T_7$ ) connected to the supply voltage. The second stage is a

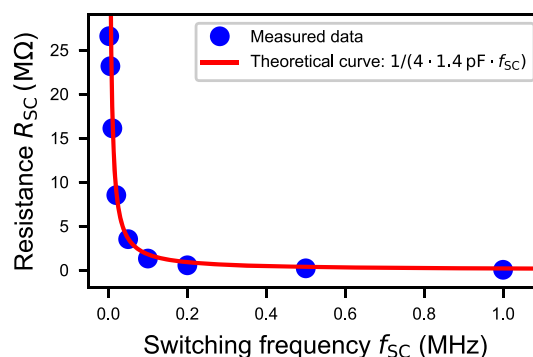
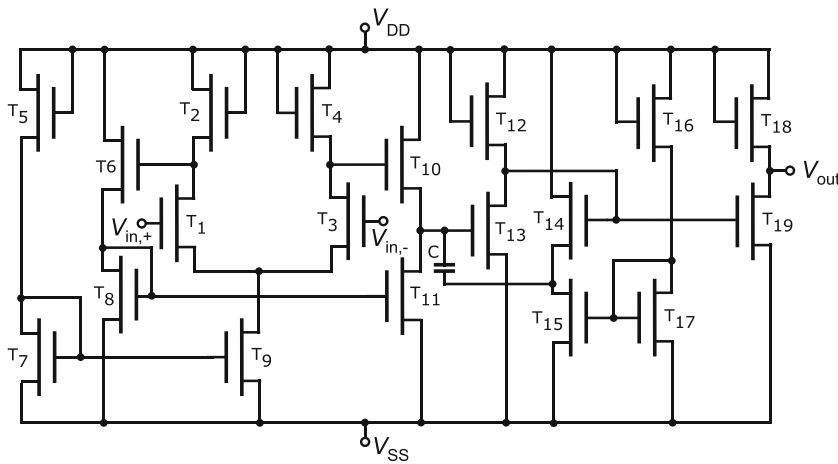


FIGURE 9 Resistance of a switched capacitor  $R_{\text{SC}}$  for switching frequencies  $f_{\text{SC}}$  between zero and 1 MHz. The capacitor has a value of  $C = 1.4 \text{ pF}$ .

differential to single stage ( $T_6, T_8, T_{10}$  and  $T_{11}$ ), which converts the output voltage of the input stage into a single signal. The next stage is an inverter realized by a pair of transistors ( $T_{12}$  and  $T_{13}$ ), which acts as an amplifier. With the help of a capacitor and a source follower ( $T_{14}, T_{15}, T_{16}$  and  $T_{17}$ ), the frequency difference between the first two poles is increased (pole splitting) which provides the unity gain stability of the operational amplifier. As output stage, a common mode amplifier is used. The output stage ( $T_{18}$  and  $T_{19}$ ) should be able to drive a large output current with a small output resistance. The Bode plot of the presented operational amplifier design has been simulated with the analog circuit simulation software AIM-Spice.<sup>15</sup> Therefore, the parameters of a-Si transistor models were modified such that their characteristics matching the produced enhancement mode a-IGZO transistors. The simulated Bode plot is illustrated in Figure 11. In the simulation, the operational amplifier has an open loop gain of  $33.58 \text{ dB}$ . The simulated cut-off frequency  $f_c$  is roughly  $1 \text{ kHz}$ , and the unity gain frequency  $f_{\text{ug}}$  has a value of  $73.6 \text{ kHz}$ . At  $221 \text{ kHz}$ , a phase shift of  $-180^\circ$  appears. The phase margin  $PM$  is  $100^\circ$ . The operational amplifier is intentionally designed with such a high phase margin to ensure the unity gain stability even if the transistor characteristics change slightly due to production imperfections. The focus is on the creation of a stable feedback able operational amplifier more than on creating an operation amplifier with a higher gain-bandwidth product. In Figure 12, the measured Bode plot of the fabricated operational amplifier is shown. It can be seen that for frequencies  $f$  lower than the cut-off frequency  $f_c$  of  $125 \text{ Hz}$ , the operational amplifier has an open loop gain  $G$  greater than or equal to  $29.51 \text{ dB}$ . At the cut-off frequency  $f_c$ , the Gain  $G$  is decreased by  $3 \text{ dB}$  from the maximum gain. A unity gain frequency  $f_{\text{ug}} = 3.4 \text{ kHz}$  can be determined. The phase difference  $P$  between input signal and output signal is



**FIGURE 10** All-enhancement thin-film transistor (TFT) operational amplifier circuit design consisting of 19 enhancement mode TFTs and a single capacitor  $C = 10$  pF.

**TABLE 1** Geometries of the TFTs used for the operational amplifier.

$w/l$ ( $\mu\text{m}$ )	TFT no.
10/50	T <sub>5</sub> , T <sub>6</sub> , T <sub>10</sub> , T <sub>12</sub> , T <sub>16</sub>
10/40	T <sub>18</sub>
10/10	T <sub>7</sub> , T <sub>9</sub> , T <sub>2</sub> , T <sub>4</sub> , T <sub>15</sub> , T <sub>17</sub> , T <sub>19</sub>
150/10	T <sub>14</sub>
200/10	T <sub>1</sub> , T <sub>3</sub> , T <sub>8</sub> , T <sub>11</sub> , T <sub>13</sub>

Abbreviation: TFT, thin-film transistor.

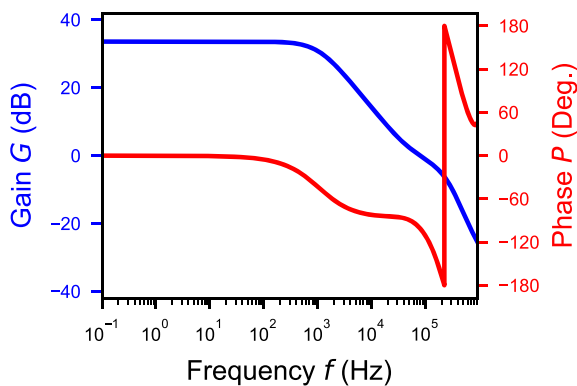


**FIGURE 11** Simulation: Gain  $G$  and phase  $P$  response of the operational amplifier dependent on the frequency  $f$ .

close to zero for frequencies  $f$  smaller than the cut-off frequency  $f_c$ . With increasing frequency  $f$ , the absolute phase lag is increasing. At a frequency of 4.1 kHz, the output signal is shifted by  $-180^\circ$  from the input signal. For higher frequencies, the negative feedback is becoming a positive feedback. The phase margin  $PM$  of the manufactured operational amplifier amounts to  $30^\circ$ . This proves the unity gain stability of the operational amplifier. It also shows the ability of the operational amplifier to be operated as a TIA with a feedback resistance

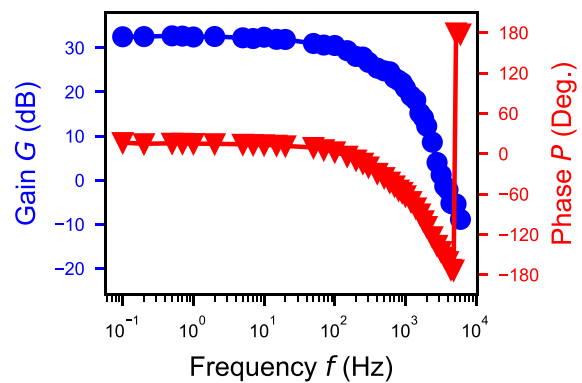


**FIGURE 12** Measured data: Gain  $G$  and phase  $P$  response of the operational amplifier dependent on the frequency  $f$ .

between inverting input node  $V_{in,-}$  and output node  $V_{out}$ . The measured amplitude characteristics show good agreement with the simulation whereas the bandwidth is decreased. The reason for this could be capacitances at line crossings. These are not included in the simulation. The biggest difference between simulation and realized operational amplifier can be seen in the phase margin. In the simulation, a phase shift of  $-180^\circ$  is reached at 221 kHz. The real-life operational amplifier reaches this point already at 4.1 kHz. This leads to a strong reduction of the phase margin. Nevertheless, the operational amplifier remains unity gain stable.

## 8 | TRANSIMPEDANCE AMPLIFIER

To realize a transimpedance amplifier, the operational amplifier is now combined with a switched capacitor which acts as feedback resistor. The output voltage  $V$  of the TIA is given by  $V = I \cdot 1 / (4 \cdot C \cdot f_{SC})$ . The  $I$ - $V$  conversion gain  $G$  and the phase response  $P$  of the TIA are

shown in Figure 13. For this measurement,  $C = 1.4$  pF and  $f_{SC} = 2.5$  kHz are used. Theoretically, this results in an  $I$ - $V$  conversion gain of  $-157.08$  dB $\Omega$ . For frequencies  $f$  smaller than 1 kHz, the measured values for  $G$  ( $-155.54$  dB $\Omega$ ) are close to the theoretical value. The small deviation between the measured value and the theoretical one can be attributed from the measuring uncertainty of 0.1 pF of the capacitor  $C$ . Moreover, the operational amplifier has a finite gain. By an open loop gain of  $G = 32.51$  dB, the real transimpedance deviates by 2.30% from the ideal case with infinite gain. The phase difference  $P$  between input current signal and output voltage signal is around  $-180^\circ$  as expected. For frequencies  $f$  larger than 1 kHz, the absolute  $I$ - $V$  conversion decreases for increasing frequency. Additionally, the absolute phase difference increases. Finally, a DC current with varying strength was applied to the input of the TIA and the output voltage was measured (Figure 14). A linear relation between input current and output voltage can be determined. With increasing input current, the output voltage decreases linearly. This proves the functionality of the transimpedance amplifier. An offset voltage

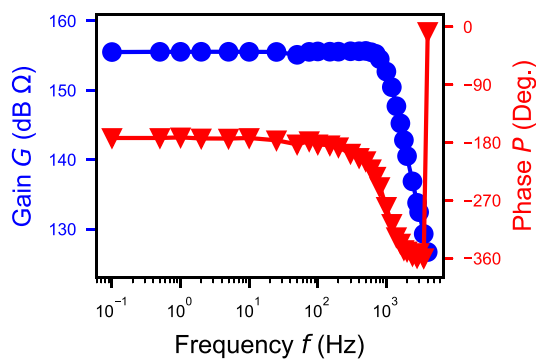


FIGURE 13 Absolute  $I$ - $V$  conversion gain  $G$  and phase  $P$  response of the transimpedance amplifier in dependence on frequency  $f$ .

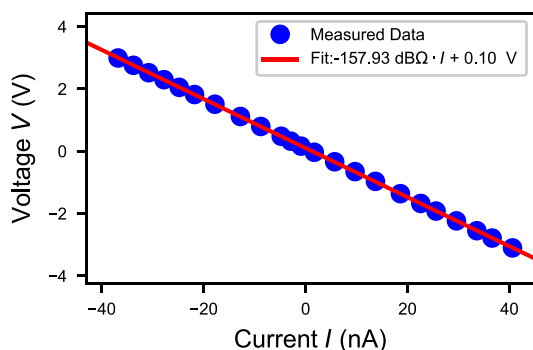


FIGURE 14 Output voltage  $V$  depending on the input current  $I$  of a transimpedance amplifier.

(input current  $I = 0$  A) of 100 mV can be determined. The reason for this voltage offset is either a mismatch of the transistors  $T_1$  and  $T_3$  or  $T_2$  and  $T_4$  of the differential amplifier stage. The coefficient between output voltage  $V$  and input current  $I$  is  $-157.93$  dB $\Omega$ . This corresponds to a resistance of 78.76 M $\Omega$ . If the TIA is set up like this, detection of currents in the nanoampere and picoampere range is possible. This enables the presented TIA to operate as the readout of the created ultraviolet photosensors.

## 9 | COMBINATION OF PHOTSENSOR AND TRANSIMPEDANCE AMPLIFIER

In the following, the results from the photosensor-transimpedance amplifier combination are illustrated. A voltage of 25 V is applied between the photosensor electrodes. The TIA is again set up in such a way that it has a  $I$ - $V$  conversion gain  $G$  of  $-157.93$  dB $\Omega$ . With this value the current of the photosensor can be calculated from the output voltage  $V$  of the TIA (Figure 14). The light source was switched on and off with a frequency  $f$  of 0.1 Hz. Figure 15 shows that if no light is hitting the photosensor, a voltage of  $-0.27$  V is measured. This corresponds to a dark current  $I_{DARK}$  of  $-3.21$  nA. If ultraviolet light

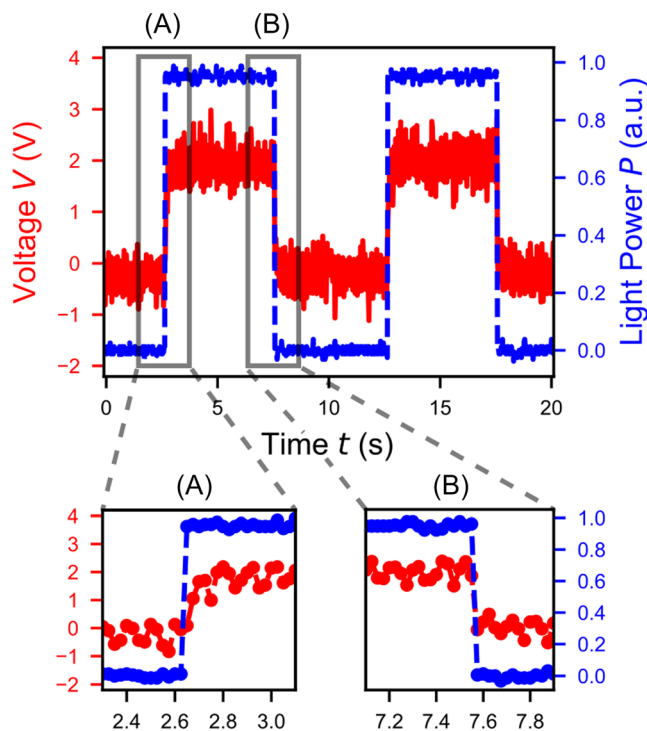


FIGURE 15 Repeating sensing property of the sensor-readout combination. The light source is switched on and off at a frequency of  $f = 0.1$  Hz.

(385 nm) is illuminating the sensor, the output voltage increases to 1.95 V (sensor current: 24.76 nA). A response time  $t_{\text{RES}}(\text{up/down}) = 30 \text{ ms}/25 \text{ ms}$  can be determined. In comparison with pn-junction diodes using silicon, this value is quite high. The reason for this is the persistent photoconductivity effect (PPC) known in a-IGZO caused by hole trapping and the ionization of oxygen bonds leading to oxygen vacancies.<sup>16</sup> If the light source would be switched with a much higher frequency  $f$ , the voltage difference between on and off state will be decreased. The sensor is not able to follow the light source fast enough. These results clearly prove the possibility to measure ultraviolet light and convert it with an on-glass transimpedance amplifier to a robust voltage. The short distance between photosensor and readout should lead to a good signal-to-noise ratio since less electronic noise is picked up. The distance can be decreased to a few micrometers when the sensor-readout combination is realized on one substrate.

## 10 | CONCLUSION

This paper presents the combination of a real-time photosensor for ultraviolet light and the readout circuit manufactured on glass substrates based on a-IGZO semiconductor technology. The photosensor is realized by an MSM-structure consisting of gold electrodes connected with a-IGZO. The readout of the sensor contains an all-enhancement TFT operational amplifier with an open loop gain  $G$  of 32.51 dB and a unity gain frequency  $f_{\text{ug}} = 3.4 \text{ kHz}$  and a switched capacitor with a temporal mean resistance  $R_{\text{SC}}$  of 78.76 M $\Omega$ . With this, the transimpedance amplifier has an  $I$ - $V$  conversion gain  $G$  of  $-157.93 \text{ dB}\Omega$ . This is enough to measure the current of the photosensor. The functionality of the photosensor-readout combination is proven, and a maximum responsivity  $R = 120 \text{ A/W}$  and a noise equivalent power  $NEP = 0.2 \text{ nW}/\sqrt{\text{Hz}}$  are measured for the photosensors. A negative point of the created photosensors is the response time  $t_{\text{RES}}(\text{up/down})$  of 30 ms/25 ms.

## 11 | OUTLOOK

Different photosensor structures and electrode material should be tested, possibly improving the response time of the photosensors. This parameter is not improved in comparison with standard silicon-based photodetection in the UV-range. Thinking of photosensor arrays, the response time of one single sensor is a limiting factor for the refresh rate. In the presented manufacturing process, the photosensors are not encapsulated. Over time, the properties of the semiconductor channel changes due to

environmental influences. To prevent this, a passivation layer should be added to the layer stack. The electrical readout can be upgraded by improving the operational amplifier characteristics. The open loop gain can be increased by using a depletion type transistor as load in the common mode amplifier. A higher open loop gain lead to a more precise current-voltage conversion. One way to improve the bandwidth of the operational amplifier is to reduce the overlap capacitances between gate/source and gate/drain of the TFTs by using a self-aligned production process. Realization of electrical readout and photosensor on the same substrate should show superior noise properties because the distance between sensor and readout are only a few micrometers. Therefore, the production of the photosensor should not influence the underlying readout circuit. The production processes can be changed such that the transistors and the photosensors use the same semiconductor channel. This would lead to a reduction of process steps and costs. A next step would also be the realization of an analog-digital-converter with a-IGZO TFTs, further improving the noise robustness of the output signal.


## ACKNOWLEDGMENTS

Y.S., P.S., H.K., T.P. and N.F. acknowledge funding by the Deutsche Forschungsgemeinschaft (DFG, German Research Foundation)-431314977/GRK2642 (Research Training Group: "Towards Graduate Experts in Photonic Quantum Technologies"). Open Access funding enabled and organized by Projekt DEAL.


## ORCID

Yannick Schellander  <https://orcid.org/0000-0002-9790-262X>

Marius Winter  <https://orcid.org/0009-0006-3646-700X>

Maurice Schamber  <https://orcid.org/0009-0008-1187-2513>

Fabian Munkes  <https://orcid.org/0000-0002-2964-813X>

Patrick Schalberger  <https://orcid.org/0000-0003-3735-3910>

Harald Kuebler  <https://orcid.org/0000-0001-5110-5337>

Tilman Pfau  <https://orcid.org/0000-0003-3272-3468>

## REFERENCES

- Zhang YY. Improved detectivity of flexible a-InGaZnO UV photodetector via surface fluorine plasma treatment. *IEEE Electron Device Lett.* 2019;40(10):1646–1649. <https://doi.org/10.1109/LED.2019.2933503>
- Chen H. New concept ultraviolet photodetectors. *Mater Today.* 2015;18(9):493–502, ISSN 1369–7021. <https://doi.org/10.1016/j.mattod.2015.06.001>
- Kopitzki K, Herzog P. *Einführung in die Festkörperphysik* Springer-Verlag; 2013 ISBN: 978–3–527-41226-6.



4. Knobelspies S. Photo-induced room-temperature gas sensing with a-igzo based thin-film transistors fabricated on flexible plastic foil. *Sensors*. 2018;18(2):358. <https://doi.org/10.3390/s18020358>
5. Zhou HT. Realization of fast-response flexible ultraviolet photodetector employing a metal-semiconductor-metal structure InGaZnO photodiode. *PSC Adv*. 2015;5(107):87993–87997. <https://doi.org/10.1039/C5RA17475A>
6. Huang C. Realization of a self-powered InGaZnO MSM UV photodetector using localized surface fluorine plasma treatment. *ACS Appl Electron Mater*. 2020;2(9):2976–2983. <https://doi.org/10.1021/acsaelm.0c00595>
7. Meng Y. A novel PbS/n-IGZO thin-film nano-photodetector with high responsivity and high photo-to-dark current ratio; 2018: 131–134. <https://doi.org/10.1109/NEMS.2018.8557018>
8. Manual FDS010 Si photodiode. Thorlabs; 2022.
9. Mackowiak V. NEP-noise equivalent power. Thorlabs; 2022.
10. Ho J. Historical introduction to capacitor technology. *IEEE Electr Insulation Mag*. 2010;26(1):20–25. <https://doi.org/10.1109/MEI.2010.5383924>
11. Temes G. Switched-capacitor filter design using the bilinear z-transform. *IEEE Trans Circ Syst*. 1978;25(12):1039–1044. <https://doi.org/10.1109/TCS.1978.1084417>
12. Kim D. On-glass operational amplifier using solution-processed a-IGZO TFTs; 2016. <https://doi.org/10.1109/APCCAS.2016.7804027>
13. Tsvividis YP. An integrated NMOS operational amplifier with internal compensation. *IEEE J Solid-State Circ*. 1976;11(6): 748–753. <https://doi.org/10.1109/JSSC.1976.1050813>
14. Dandekar M. An a-IGZO TFT based Op-Amp with 57 dB DC-Gain, 311 KHz Unity-gain Freq., 75 deg. Phase margin and 2.43 mW power on flexible substrate. *ESSCIRC 2021 - IEEE 47th European Solid State Circuits Conference (ESSCIRC)*, Grenoble, France; 2021: 407–410. <https://doi.org/10.1109/ESSCIRC53450>
15. Aim-spice reference manual version 2017.100; 2017.
16. Jang JT. Effects of structure and oxygen flow rate on the photo-response of amorphous IGZO-based photodetector devices. *Solid-State Electron*. 2018;140:115–121, ISSN 0038–1101. <https://doi.org/10.1016/j.sse.2017.10.028>

## AUTHOR BIOGRAPHIES



**Yannick Schellander** is a PhD student at the Institute for Large Area Microelectronics, University of Stuttgart. He received a bachelor degree in physics at the 5th Institute of Physics, where he was working on the realization of a laser stabilization for a quantum gas experiment. His master's thesis was on the topic of measuring ionization currents of Rydberg states in nitric oxide created by continuous-wave three-photon excitation. Mr. Schellander's current work is focused on non-visible spectrum optical

sensing and current detection using the semiconductor material amorphous indium gallium zinc oxide.



**Marius Winter** is a Master student at the Institute for Large Area Microelectronics at the University of Stuttgart. He got his Bachelor's degree for his work on representation learning using contrastive self-supervised learning at the Institute for Signal Processing and System Theory. His Master's thesis is dealing with the development of operational amplifiers with indium-gallium-zinc-oxide thin-film transistors.



**Maurice Schamber** is a Master's student at the 5th Institute of Physics at the University of Stuttgart. During his Bachelor thesis, he was working on ellipsometric characterizations on hard coatings at the 1st Institute of Physics. At the moment, he is dealing with non-visible spectrum optical sensing with amorphous indium-gallium-zinc-oxide, specifically the integration of photosensor arrays for ultraviolet light into vapor cells.



**Fabian Munkes** is a PhD student at the 5th Institute of Physics at the University of Stuttgart. He received his Bachelor's degree for designing a frequency modulation system for spectroscopy in optically thin alkali gasses. He then joined Prof. James P. Shaffer's research group at the University of Oklahoma, USA, for 5 months leading to the publication *Phys. Rev. Lett.* 122, 103001 (2019). Back in Stuttgart, his Master's thesis was on continuous-wave absorption spectroscopy on the X 2Π<sub>1/2</sub> to A 2Σ<sup>+</sup> transition of nitric oxide. Mr. Munkes's current work is focused on the creation of a trace gas sensor for nitric oxide.



**Dr. Patrick Schalberger** studied Electrical Engineering at the University of Stuttgart. He received his diploma degree in 2005 and his doctoral degree in 2012. Since then he has led or administrated several research projects covering various aspects of display manufacturing. His current research interests include the development of advanced driving circuits for system-on-panel (SOP) displays and surface MEMS applications.



**Dr. Harald Kuebler** is a research group leader at the 5th institute of Physics at the University of Stuttgart. He obtained his PhD in physics for his research on Rydberg spectroscopy in a rubidium microcell at the same institute. During his Postdoc at the University of Oklahoma, he participated in the development of vapor cell-based microwave sensing. Since that time, his research focus lies on Rydberg based quantum sensors by joining the fields of physics and electrical engineering.



**Prof. Tilman Pfau** is a full professor holding a chair in photonics. Important steps in his vita were the reception of his PhD at the University of Konstanz in the group of Prof. J. Mlynek. In 1998, he received his habilitation on the topic light in atomic physics. In 2000, he founded and became head of the 5th Institute of Physics, which conducts research in the fields of dipolar quantum gasses, Rydberg state physics, quantum optics with hot atoms and quantum computing. During his academic carrier, Prof. Pfau received a high number of significant awards including the Rudolf Kaiser Prize and the Herbert P. Broida Prize of the American Physical Society.



**Prof. Norbert Fruehauf** received his Ph.D. (Dr-Ing.) in Electrical Engineering from the University of Stuttgart, Germany, and has more than 30 years of experience in designing and characterizing liquid crystal light modulators and displays. From 1998

to 2001, he worked for Physical Optics Corporation, Torrance, California, USA, where he developed tunable micro-optic components, various display systems, and integrated optical components. In 2001, he was appointed full professor heading the Chair of Display Technology at the University of Stuttgart, Germany, where he specializes in large area microelectronics for applications in flexible displays, AMOLEDs and AMLCDs and sensor arrays. Prof. Fruehauf is the inventor of the active matrix OLED pixel circuit with external compensation used in all worldwide sold active matrix OLED TVs, which was licensed to LG Display in 2021. He has been General Chair of the SID Symposium 2014, Program Chair of Eurodisplay 2009, SID Symposium 2014, and Eurodisplay 2022 and serves on various other international Conference Organizing Committees such as AMFPD and IDW. He is the current SID Regional Vice President Europe.

**How to cite this article:** Schellander Y, Winter M, Schamber M, Munkes F, Schalberger P, Kuebler H, et al. Ultraviolet photodetectors and readout based on a-IGZO semiconductor technology. *J Soc Inf Display*. 2023;31(5):363–72. <https://doi.org/10.1002/jsid.1202>